J. Fluid Mech. (2008), *vol.* 605, *pp.* 1–18. © 2008 Cambridge University Press
doi:10.1017/S0022112008001092 Printed in the United Kingdom

Two-dimensional and axisymmetric viscous flow in apertures

SADEGH DABIRI[1], WILLIAM A. SIRIGNANO[1] AND DANIEL D. JOSEPH[1,2]

[1]Department of Mechanical and Aerospace Engineering, University of California, Irvine, CA 92697, USA
[2]Department of Aerospace Engineering and Mechanics, University of Minnesota, Minneapolis, MN 55455, USA

(Received 28 June 2007 and in revised form 17 February 2008)

The flow in a plane liquid jet from an aperture is obtained by direct simulation of the Navier–Stokes equations. The gas–liquid interface is tracked using the level set method. Flows are calculated for different Reynolds and Weber numbers. When $We = \infty$, the maximum value of the discharge coefficient appears around $Re = O(100)$. The regions that are vulnerable to cavitation owing to the total stress are identified from calculations based on Navier–Stokes equations and viscous potential flow; the two calculations yield similar results for high Reynolds numbers. We prove that the classical potential flow solution does not give rise to a normal component of the rate of strain at the free streamline. Therefore, the normal component of the irrotational viscous stresses also vanishes and cannot change the shape of the free surface. The results of calculations of flows governed by the Navier–Stokes equations are close to those for viscous potential flow outside the vorticity layers at solid boundaries. The Navier–Stokes solutions for the axisymmetric aperture are also given for two values of Reynolds numbers. The results for axisymmetric and planar apertures are qualitatively similar, but the axisymmetric apertures have a lower discharge coefficient and less contraction.

1. Introduction

High-pressure atomizers and spray generators are of great interest in industry. They have many applications such as fuel injectors, pharmaceutical sprays and agricultural sprays.

It is known that generally the liquid/air interaction is very important in the breakup of liquid jets. However, experimental studies by Tamaki *et al.* (1998, 2001) and Hiroyasu (2000) show that the disturbances inside the nozzle caused by the collapse of travelling cavitation bubbles make a substantial contribution to the breakup of the exiting liquid jet. Even with high-pressure drops, the main flow of a liquid jet does not atomize greatly when a disturbance caused by cavitation is not present. Nurick (1976) also observed that the presence of cavitation in a nozzle will decrease the uniformity of the mixing for unlike impinging doublets. He & Ruiz (1995) studied the effect of cavitation on turbulence in flows through plain orifices. They measured the velocity field for both cavitating and non-cavitating flow in the same geometry. They observed that the impingement of the free-surface flow onto the orifice wall increases the turbulence generation behind the cavity. Also, turbulence in the cavitating flow is higher and decays more slowly than in the non-cavitating flow.

https://doi.org/10.1017/S0022112008001092 Published online by Cambridge University Press

Many numerical studies have been performed on the cavitation inside the orifice flow (Xu, Heister & Blaisdell 2004; Chen & Heister 1996; Bunnell & Heister 2000). Bunnell *et al.* (1999) studied the unsteady cavitating flow in a slot. They found that partially cavitated slots undergo a periodic oscillation when the Strouhal number is near one. The Strouhal number is based on orifice length and Bernoulli velocity. Different models for two-phase flow and cavitation have been used in the past. For example, Kubota, Kato & Yamaguchi (1992) derived a constitutive equation for the pseudo-density from the Rayleigh–Plesset equation for bubble dynamics. These models are based on pressure, and neglect viscous stresses. In the present work, we consider the effects of viscous stresses.

Many experimental studies of cavitation can be found in the literature. Mishra & Peles (2005*a*,*b*) looked at the cavitation in flow through a micro-orifice inside a silicon microchannel. Payri *et al.* (2004) studied the influence of cavitation on the internal flow and the spray characteristics in diesel injection nozzles. Ahn, Kim & yoon (2006) studied the effects of cavitation and hydraulic flip on the breakup of a liquid jet injected perpendicularly into subsonic crossflow. They showed that cavitation shortens the length at which a liquid column will break up. Jung, Khil & Yoon (2006) considered the breakup characteristics of liquid sheets formed by a like-doublet injection. They found that turbulence delays sheet breakup and shortens the wavelength of both ligaments and sheets. Ganippa *et al.* (2004) considered the cavitation growth in the nozzle as they increased the flow rate. First, travelling bubbles are created. These bubbles are detached from the wall and move with the stream. By increasing the flow, an unsteady cloud of cavitation is observed. Further increase of the flow rate causes a non-symmetrical distribution of cavitation within the nozzle and its extension to the nozzle exit. More atomization occurs at the side with stronger cavitation.

The dynamics of liquid sheets has also been extensively described in the literature. These sheets are important in atomization and spray combustion (Lefebvre 1989) and curtain coating (Brown 1961). Jets created by slot atomizers are close to two-dimensional flows.

Flow through an aperture is a simple example of flow with hydraulic flip that occurs in nozzles with sharp corners. In experiments on cavitating orifices, the occurrence of hydraulic flip coincides with the disappearance of cavitation bubbles and increase in the breakup length of the jet (e.g. Tamaki *et al.* 1998). However, the present work shows that cavitation is possible in hydraulically flipped flows, especially in the case of low Reynolds numbers where the viscous stress is significant.

In this paper, we are interested in the idea that cavitation can induce the formation of detached vapour bubbles that travel with the liquid.

According to the traditional criterion, cavitation occurs when the pressure drops below the breaking strength of liquid. This threshold value depends on the type of nucleation. In the homogeneous nucleation, the nucleation sites are temporary microscopic voids that are associated with thermal motion within the liquid. In this case, the critical pressure could be much lower than the vapour pressure. However, in heterogeneous nucleation, which occurs in most engineering situations, rupture occurs at the boundary between the liquid and solid, or between liquid and small solid particles suspended in the liquid. In this case, rupture could occur at pressures closer to the vapour pressure. It can be argued that in the case of heterogeneous cavitation, which depends so critically on impurities and sample preparation, the opening of cavitation in a liquid is better described by the words 'breaking strength' than by the thermodynamics of ideal phase, change of liquid/vapour in equilibrium.

https://doi.org/10.1017/S0022112008001092 Published online by Cambridge University Press

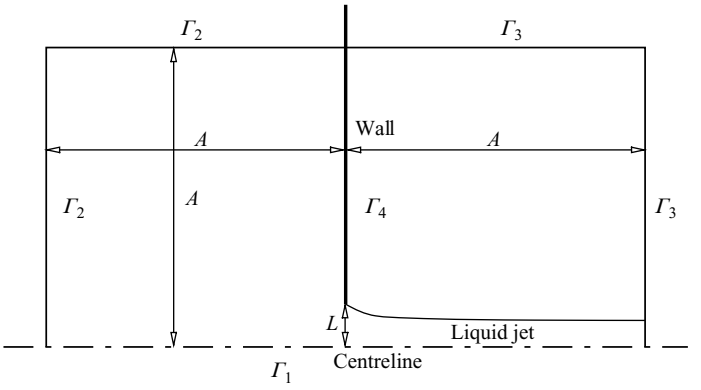


FIGURE 1. Geometry of the computational domain.

The action of viscous stresses is definitely non-equilibrium; we are using 'cavitation' in the sense of rupture of liquids not following exactly laws of liquid/vapour equilibrium.

Joseph (1998) proposed that cavitation can be induced by the total stress, which includes both the pressure and the viscous stress. Cavitation occurs when the maximum principal stress drops below the breaking strength of liquid. Using this criterion, Funada, Wang & Joseph (2006) predicted cavitation of a two-dimensional steady viscous potential flow through an aperture. Also, for axisymmetric viscous flow through an orifice, Dabiri, Sirignano & Joseph (2007) predicted cavitation using Joseph's total-stress criterion to post-process the solutions of the Navier–Stokes equations. These papers take a common approach although the configurations vary widely. Based on this new criterion, the inception of cavitation at each point in the field is determined. If cavitation does occur, the flow field can be drastically changed. This approach is similar to that used in the analysis of hydrodynamic stability in which the field at risk of instability is very different from the one that develops after the onset of instability.

The theory of stress-induced cavitation aims to explain the phenomenon of cavitation observed in moving liquid undergoing strain. This theory modifies the classical theory which uses only pressure for the cavitation criterion. Now, the total stress, including the tensile contribution from viscous stress, is included. So, the theory is intended to improve the understanding and predictive capability for cavitation in liquids undergoing strain due to motion.

Except for Dabiri *et al.* (2007), previous calculations on high-pressure-nozzle cavitation have used the traditional criterion. The purpose of this paper is to use the new criterion to study cavitation in aperture flow.

2. Theoretical development

2.1. *Navier–Stokes flow*

In this study, we consider flow of a liquid leaving an aperture in a flat plate and creating a jet in a stagnant gas. The physical problem and the computational domain are shown in figure 1, where A is the size of the computational domain and L is the half-width of the aperture. The Navier–Stokes equations for an incompressible viscous flow are

$$\rho_i \left(\frac{\partial \boldsymbol{u}}{\partial t} + \boldsymbol{u} \cdot \nabla \boldsymbol{u} \right) = -\nabla p + \nabla \cdot (2\mu_i \boldsymbol{D}) + \sigma \kappa \delta(d) \boldsymbol{n}, \tag{2.1}$$

https://doi.org/10.1017/S0022112008001092 Published online by Cambridge University Press

$$\boldsymbol{D} = \frac{1}{2}\left[(\nabla \boldsymbol{u}) + (\nabla \boldsymbol{u})^{\mathbf{T}}\right], \tag{2.2}$$

$$\nabla \cdot \boldsymbol{u} = 0, \tag{2.3}$$

where $\boldsymbol{u}$, ρ and μ are the velocity, density and viscosity of the fluid, respectively. Subscript i could represent either liquid or gas phase and $\boldsymbol{D}$ is the strain rate tensor. The last term represents the surface tension as a force concentrated on the interface. Here, σ is the surface tension coefficient, κ is the curvature of the interface, and δ is the Dirac delta function. d represents the distance from the interface and $\boldsymbol{n}$ corresponds to the unit normal vector at the interface. The flow is characterized by the gas-to-liquid density ratio, viscosity ratio and non-dimensional parameters: Reynolds number (Re) and Weber number (We), which are defined as follows:

$$Re = \frac{\rho_{liq} U L}{\mu_{liq}}, \quad We = \frac{\rho_{liq} U^2 L}{\sigma}, \quad \rho\text{-ratio} = \frac{\rho_{gas}}{\rho_{liq}}, \quad \mu\text{-ratio} = \frac{\mu_{gas}}{\mu_{liq}}, \tag{2.4}$$

$$U = \sqrt{\frac{2(p_u - p_d)}{\rho_{liq}}}, \tag{2.5}$$

where L is the half-width of the aperture, U is the Bernoulli velocity of jet and p_u and p_d are the upstream and downstream pressures, respectively.

After finding the velocities and pressure field, we can calculate the stress tensor using

$$\boldsymbol{T} = \mu\left[(\nabla \boldsymbol{u}) + (\nabla \boldsymbol{u})^{T}\right] - p\boldsymbol{I} \tag{2.6}$$

where $\boldsymbol{I}$ is the identity matrix and superscript T refers to transpose of a tensor. In the planar flow the stress tensor has the following form

$$\boldsymbol{T} = \begin{bmatrix} T'_{11} & T'_{12} & 0 \\ T'_{21} & T'_{22} & 0 \\ 0 & 0 & 0 \end{bmatrix}, \tag{2.7}$$

Therefore, the maximum tensile stress, T_{11} can be calculated using the planar stress analysis in the (x, y)-plane:

$$T_{11} = \frac{T'_{11} + T'_{22}}{2} \pm \sqrt{\left(\frac{T'_{11} - T'_{22}}{2}\right)^2 + T'^2_{12}}. \tag{2.8}$$

The total-stress criterion is used to find regions in the flow at risk of cavitation. According to this criterion, cavitation occurs when the maximum principal stress exceeds the negative of the critical threshold pressure of liquid at local temperature, i.e.

$$T_{11} > -p_c. \tag{2.9}$$

The critical threshold pressure, p_c, might be the vapour pressure, p_v, or some other value determined by sample preparation. The dimensionless cavitation number, K, defines the critical threshold pressure, p_c,

$$K = \frac{p_u - p_d}{p_d - p_c}. \tag{2.10}$$

2.2. *Interface tracking and level-set formulation*

Several methods have been proposed and implemented to capture the interface, and model the surface tension in a two-phase flow; these include the front-tracking method

https://doi.org/10.1017/S0022112008001092 Published online by Cambridge University Press

by Tryggvason *et al.* (2001) and volume of fluid method by Hirt & Nichols (1981). Also, Popinet & Zaleski (1999) did an accurate balance of surface tension forces in a finite, volume method by explicit tracking of the interface. See Scardovelli & Zaleski (1999) for a review of different methods of interface tracking and surface tension modelling.

We are considering incompressible flow of two immiscible fluids. The interface between these fluids moves with the local velocity of the flow field. To track the motion of the interface the level-set method is used which has been developed by Osher and coworkers (e.g. Sussman *et al.* 1998; Osher & Fedkiw 2001). The level-set function, denoted by θ, is defined as a signed distance function. It has positive values on one side of the interface (gas phase), and negative values on the other side (liquid phase). The magnitude of the level set at each point in the computational field is equal to the distance from that point to the interface.

The level-set function is convected by the flow as a passive scalar variable:

$$\frac{\partial \theta}{\partial t} + \boldsymbol{u} \cdot \nabla \theta = 0. \tag{2.11}$$

It is obvious that, if the initial distribution of the level set is a signed distance function, after a finite time of being convected by a non-uniform velocity field, it will not remain a distance function. Therefore, we must re-initialize the level-set function so it will be a distance function (with property of $|\nabla\theta| = 1$) without changing the zero level set (position of the interface).

Suppose $\theta_0(\boldsymbol{x})$ is the level-set distribution after some time step and is not exactly a distance function. This can be re-initialized to a distance function by solving the following partial differential equation (Sussman *et al.* 1998):

$$\frac{\partial \theta'}{\partial \tau} = \mathrm{sign}(\theta_0)(1 - |\nabla \theta'|) \tag{2.12}$$

with initial conditions:

$$\theta'(\boldsymbol{x}, 0) = \theta_0(\boldsymbol{x}) \tag{2.13}$$

where

$$\mathrm{sign}(\theta) = \begin{cases} -1 & \text{if} \quad \theta < 0, \\ 0 & \text{if} \quad \theta = 0, \\ 1 & \text{if} \quad \theta > 0, \end{cases} \tag{2.14}$$

and τ is a pseudo-time. The steady solution of (2.12) is the distance function with property $|\nabla\theta| = 1$ and since $\mathrm{sign}(0) = 0$, then θ' has the same zero level set as θ_0.

Now the fluid properties can be defined based on the level set:

$$\begin{aligned} \rho &= \rho_{liq} + (\rho_{gas} - \rho_{liq}) H_\epsilon(\theta), \\ \mu &= \mu_{liq} + (\mu_{gas} - \mu_{liq}) H_\epsilon(\theta), \end{aligned} \tag{2.15}$$

where H_ϵ is a Heaviside function that is numerically approximated by a smooth jump:

$$H_\epsilon = \begin{cases} 0 & (\theta < -\epsilon) \\ (\theta + \epsilon)/(2\epsilon) + \sin(\pi\theta/\epsilon)/(2\pi) & (|\theta| \leqslant \epsilon) \\ 1 & (\theta > \epsilon) \end{cases} \tag{2.16}$$

ϵ represents the numerical thickness of the interface and has the value of 1.5 times the cell size. This Heaviside function corresponds to a delta function that can be used

https://doi.org/10.1017/S0022112008001092 Published online by Cambridge University Press

to evaluate the force caused by surface tension:

$$\delta_\epsilon = \begin{cases} [1+\cos(\pi\theta/\epsilon)]/(2\epsilon) & \text{if } |\theta| \leqslant \epsilon, \\ 0 & \text{otherwise,} \end{cases} \tag{2.17}$$

The last term in the momentum equation (2.1) includes the normal unity vector and the curvature of the interface which can be calculated as follows:

$$\boldsymbol{n} = \frac{\nabla\theta}{|\nabla\theta|}, \quad \kappa = -\nabla\cdot\boldsymbol{n} \tag{2.18}$$

Expansion of (2.18) in Cartesian coordinates leads to:

$$\kappa = \frac{\theta_y^2\theta_{xx} - 2\theta_x\theta_y\theta_{xy} + \theta_x^2\theta_{yy}}{\left(\theta_x^2+\theta_y^2\right)^{3/2}}. \tag{2.19}$$

2.3. *Viscous potential flow*

An inviscid approximation has been used widely in the literature to treat the flow problems with finite viscosity. For example, Moore (1965) studied the rise of a deformed bubble in a liquid of small viscosity by calculating the dissipation of an irrotational flow around the bubble. Also, Joseph & Wang (2004) considered the viscous potential flow for decay of surface gravity waves. The viscous potential flow satisfies the Navier–Stokes equations, but does not satisfy the boundary condition for the tangential component of the velocity at a rigid surface and the tangential component of shear at a free surface.

In the Appendix, it is shown that the potential flow solution of flows with free streamline satisfies the normal stress boundary condition on the free streamline in the case of finite viscosity. Therefore, the viscous potential flow solution will be used here as a comparison to the Navier–Stokes solution of the aperture problem. The problem of incompressible potential flow through an aperture was solved a long time ago. The complex potential in the z-plane for this flow is given implicitly by Currie (1974, p. 129)

$$f(z) = \phi + \mathrm{i}\psi = -\frac{2C_cLU}{\pi}\ln\left\{\cosh\left[\ln\left(U\frac{\mathrm{d}z}{\mathrm{d}f}\right)\right]\right\} - \mathrm{i}C_cLU \tag{2.20}$$

where L is half-width of the aperture and C_c is the coefficient of contraction. Funada *et al.* (2006) analysed the viscous potential flow solution of the aperture flow. The velocity field can be derived from the potential function as follows:

$$u = \frac{1}{2}\left(\frac{\mathrm{d}f}{\mathrm{d}z} + \frac{\mathrm{d}\overline{f}}{\mathrm{d}\overline{z}}\right), \quad v = \frac{\mathrm{i}}{2}\left(\frac{\mathrm{d}f}{\mathrm{d}z} - \frac{\mathrm{d}\overline{f}}{\mathrm{d}\overline{z}}\right), \tag{2.21}$$

and from there, the rate of strain tensor can be calculated:

$$2\boldsymbol{D} = \begin{bmatrix} \left(\dfrac{\mathrm{d}^2f}{\mathrm{d}z^2} + \dfrac{\mathrm{d}^2\overline{f}}{\mathrm{d}\overline{z}^2}\right) & \mathrm{i}\left(\dfrac{\mathrm{d}^2f}{\mathrm{d}z^2} - \dfrac{\mathrm{d}^2\overline{f}}{\mathrm{d}\overline{z}^2}\right) \\ \mathrm{i}\left(\dfrac{\mathrm{d}^2f}{\mathrm{d}z^2} - \dfrac{\mathrm{d}^2\overline{f}}{\mathrm{d}\overline{z}^2}\right) & -\left(\dfrac{\mathrm{d}^2f}{\mathrm{d}z^2} + \dfrac{\mathrm{d}^2\overline{f}}{\mathrm{d}\overline{z}^2}\right) \end{bmatrix}. \tag{2.22}$$

In order to calculate the maximum tension, the principal stresses should be found. The diagonalized rate of strain tensor is

$$2\boldsymbol{D} = \begin{bmatrix} \lambda & 0 \\ 0 & -\lambda \end{bmatrix}, \quad \lambda = 2\left|\frac{\mathrm{d}^2f}{\mathrm{d}z^2}\right|. \tag{2.23}$$

https://doi.org/10.1017/S0022112008001092 Published online by Cambridge University Press

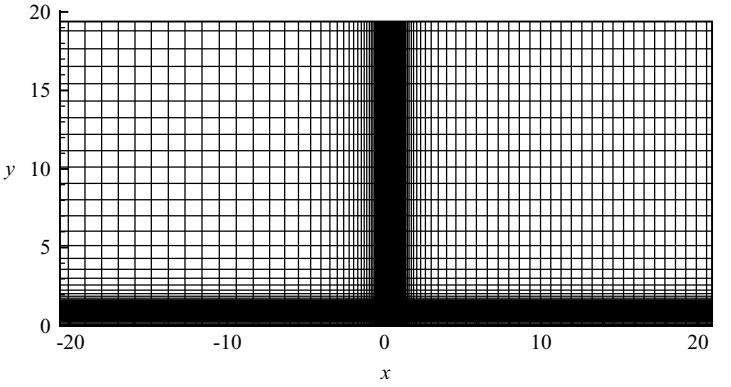


FIGURE 2. Computational domain and the Cartesian grid that is used.

Therefore, the maximum tension T_{11} is given by

$$T_{11} = -p + \mu\lambda = -p_u + \frac{1}{2}\rho(u^2 + v^2) + \mu\lambda. \tag{2.24}$$

3. Numerical implementation

The numerical solution of the incompressible unsteady Navier–Stokes equations is performed using the finite-volume method on a staggered grid. The convective and advective terms are discretized using the quadratic upwind interpolation for convective kinematics (QUICK) (Hayase, Humphrey & Greif 1992). The semi-implicit method for pressure-linked equation (SIMPLE), developed by Patankar (1980), is used to solve the pressure-velocity coupling. The time integration is accomplished using the second-order Crank–Nicolson scheme. The calculation is done for different Reynolds numbers.

The computational domain is shown in figure 1. The size of the domain is $A = 20L$ and a Cartesian grid with 77 924 nodes and 77 361 elements is employed. A non-uniform distribution of grids is used with clustering in the region of rapid velocities near the tip of the aperture. The size of the smallest elements is $\Delta x/L = 0.001$. Figure 2 shows the Cartesian grid used. The following boundary conditions are applied: Γ_1 is the axis of symmetry and the v-velocity is zero, also the normal derivative of all other variables vanishes. On the upstream boundary Γ_2, the stagnation pressure is specified as the boundary condition. On the downstream boundary Γ_3 the static pressure is specified. On the aperture plate Γ_4, all the velocity components are set to zero.

The dependence of the solution on the size of the domain is investigated. In order to ensure the accuracy of the constant pressure boundary conditions, a larger domain is considered with $A = 30L$. Comparing the results for $Re = 100$ shows that the difference in discharge coefficient is below 0.002%. In addition, calculation is done for a finer grid with the total number of nodes being doubled while keeping the same grid distribution. Comparison between two calculations for $Re = 1000$ has shown that discharge coefficients for the two cases differ by less than 0.1%.

In order to compare the results with the theoretical viscous potential flow solution, a dynamically inactive environment is required. This has been achieved by decreasing the viscosity and density of the gaseous phase. In the case with ρ-ratio and μ-ratio of 10^{-4} each, the flow becomes independent of any further decrease in these parameters. Therefore, the calculations are performed for these ratios.

https://doi.org/10.1017/S0022112008001092 Published online by Cambridge University Press

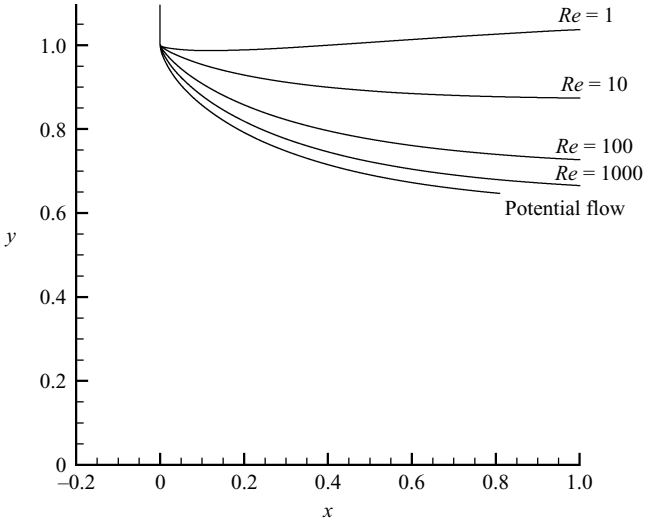


FIGURE 3. Free streamlines from the Navier–Stokes solution for $Re = 1, 10, 100, 1000$ and for potential flow. ρ-ratio $= 10^{-4}$ and μ-ratio $= 10^{-4}$.

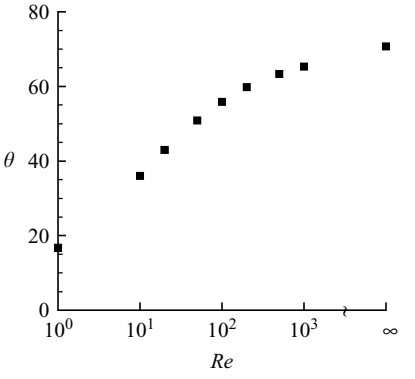


FIGURE 4. Angle between the free surface and axis of symmetry at $x/L = 0.005$.

3.1. *Effects of Reynolds number*

Figure 3 shows the free streamline (liquid–gas interface) for flows with different Reynolds numbers. It can be seen that the free streamline leaves the aperture wall at different angles for different Reynolds numbers. This angle is plotted versus Reynolds number in figure 4.

Figure 5(a) shows the thickness of jet at a distance of $5L$ downstream from the aperture. As the Reynolds number decreases, the jet thickness increases. This is because increasing the thickness of the boundary layer and decreasing the velocity causes the flow to change direction faster. For a Reynolds number of one, the jet expands. Expansion of Newtonian liquid jets has been observed before, for example by Middleman & Gavis (1961). The discharge coefficient of the aperture is plotted in figure 5(b). The value of C_d has a peak for $Re = O(100)$. As the Reynolds number decreases from infinity, the thickness of the jet increases, causing an increase in the discharge coefficient; but for very low Reynolds numbers, the velocity of the jet drops, therefore, the discharge coefficient decreases.

https://doi.org/10.1017/S0022112008001092 Published online by Cambridge University Press

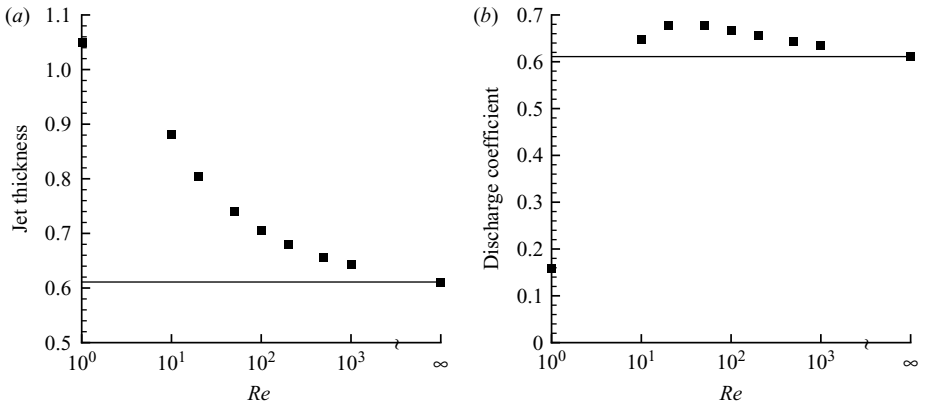


FIGURE 5. (*a*) Half-thickness of the jet normalized by L and (*b*) the discharge coefficient for different Reynolds numbers: ■, Navier–Stokes; ——, viscous potential flow.

Pressure distribution for Navier–Stokes and potential solutions is shown in figure 6 for different Reynolds numbers. (The potential flow solution for lower values of Re is not shown to avoid complexity.) For higher Reynolds numbers, the difference between Navier–Stokes and potential solutions is small. However, for lower Reynolds numbers, the pressure field deviates from potential flow. Figure 7 shows the viscous stress in the flow and compares it with the viscous potential flow case. There is a good agreement between them for $Re = 1000$ except in the wall boundary layer. Comparing figures 6 and 7, we can see that the viscous stress is two to three orders of magnitude smaller than the local pressure drop for the two higher values of Reynolds number. However, for lower Reynolds numbers, such as $Re = 10$ or 1, the viscous stress is of the same order as the local pressure drop.

It is important to note that the Reynolds number in these calculations is based on the Bernoulli jet velocity, which is larger than the actual average velocity of the jet, especially for low Reynolds numbers. For example, for flow with $Re = 1$, the jet velocity is about 20% of the Bernoulli velocity. This causes the strain rates, and therefore, the stresses to be scaled down by the same ratio. This has the significant effect of producing smaller regions of high stresses in the Navier—Stakes solution as seen in figure 7(*d*).

The total stress is calculated and compared with the threshold stress. The regions in which the cavitation criterion is satisfied are identified.

The aperture flow is always hydraulically flipped; so, the acceleration of the liquid near the exit corner is not large and the local pressure drop is not significant. Therefore, the chance of having cavitation is related to the contribution of viscous stress in the total stress tensor. Figure 8 shows the regions at risk of cavitation in different flows with the same Reynolds number and different cavitation numbers, K, corresponding to different values of critical pressure, p_c. Although the existence of cavitation bubbles could change the flow field, these bubbles cannot persist far downstream from the inception point where conditions favourable to cavitation have disappeared and the bubbles collapse. We have shown that aperture flows at low Reynolds numbers may cavitate owing to viscous stresses under conditions, such as hydraulic flip, which are unfavoarable to cavitation under the conventional criterion. The experiments on hydraulic flip are carried out for high Reynolds numbers; the

https://doi.org/10.1017/S0022112008001092 Published online by Cambridge University Press

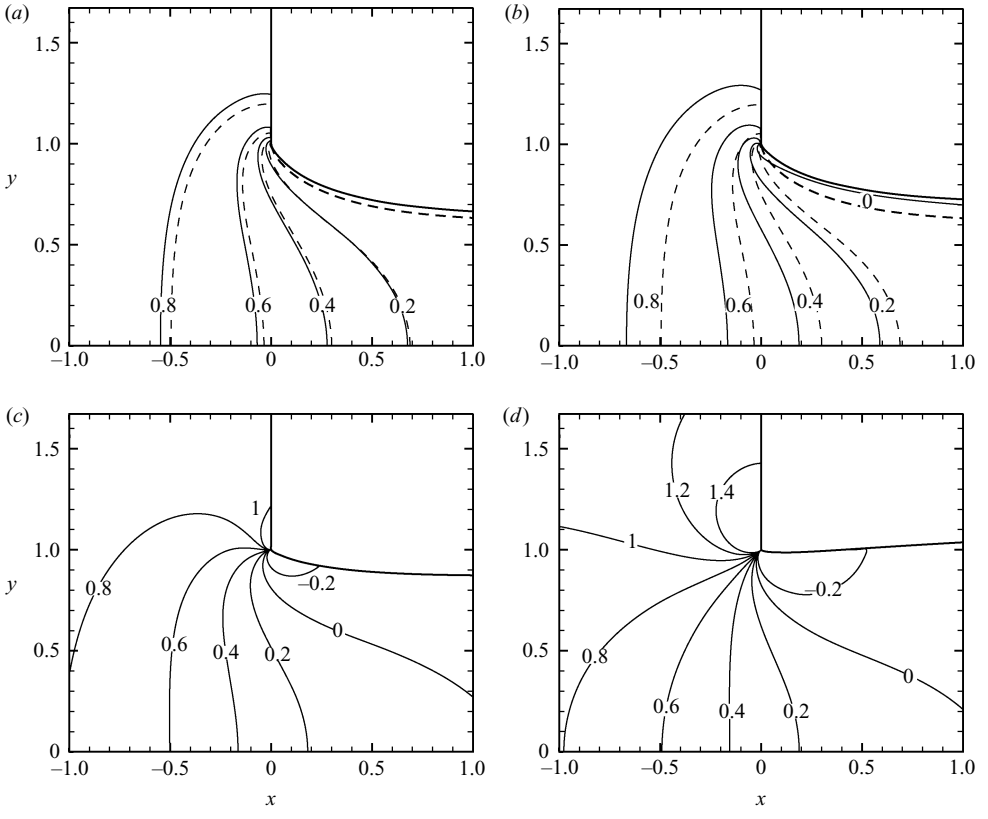


FIGURE 6. Contours of $(p - p_d)/\frac{1}{2}\rho_{liq}U^2$ for the Navier–Stokes solution (solid lines) compared to the viscous potential flow solution (dashed lines) for ρ-ratio $= 10^{-4}$ and μ-ratio $= 10^{-4}$. (*a*) $Re = 1000$, (*b*) 100, (*c*) 10, (*d*) 1 (potential flow solutions are not shown in (*c*) and (*d*)).

possible cavitation of flipped flows at low Re, owing to viscous stresses has not been studied before.

Figure 9 shows how the area of the region vulnerable to cavitation will increase as the cavitation number increases. For a specific value of K, the cavitating domain is larger for a lower Reynolds number because the viscous stress is stronger. This agrees with the statement by Padrino *et al.* (2007) about the increase in the risk of cavitation for more viscous fluids.

Another important point about figure 9 is that, for larger Reynolds numbers, the difference between the cavitating domain predicted by Navier–Stokes solution and VPF solutions will be greater. That is, for larger Reynolds numbers, the cavitation area is confined to shear layers and boundary layers which are not present in the potential flow solution.

Calculations were also done for the round aperture assuming an axisymmetric flow. A schematic of the flow is shown in figure 10. The results of these calculations are shown in figure 11. The pressure contours in the round aperture (figure 11*a*) are confined to a more compact region than in the planar flow shown in figure 6(*b*). Flow acceleration occurs in a smaller region and gives rise to a higher strain rate and viscous stress in the round aperture, as shown in the viscous stress plots in figures 11(*c*) and 7(*b*).

https://doi.org/10.1017/S0022112008001092 Published online by Cambridge University Press

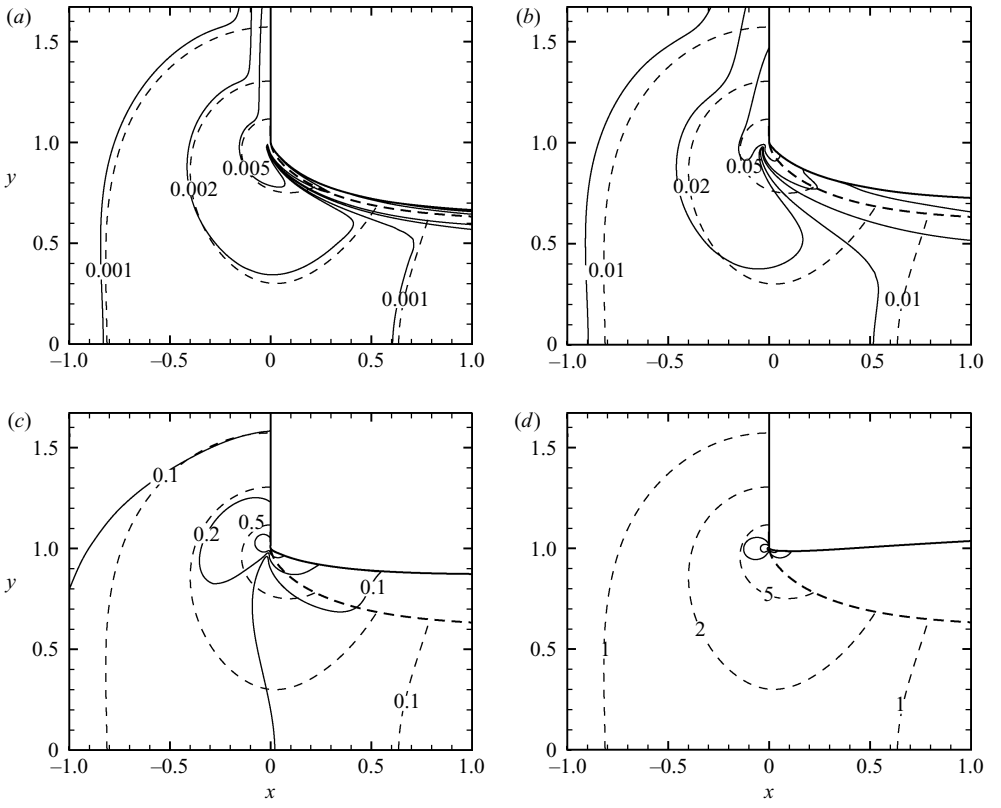


FIGURE 7. Contours of $(T_{11}+\rho)/\frac{1}{2}\rho_{liq}U^2$ for the Navier–Stokes solution (solid lines) compared to the viscous potential flow solution (dashed lines) for ρ-ratio $= 10^{-4}$ and μ-ratio $= 10^{-4}$. (*a*) $Re = 1000$, (*b*) 100, (*c*) 10, (*d*) 1.

3.2. *Effects of Weber number*

The flows for Weber numbers of 10, 100, 1000 and infinity are calculated and the free streamlines are shown in figure 12. The flow with a Weber number of 1000 is very close to the flow with no surface tension, or infinite Weber number. The free stream for these two cases cannot be distinguished in these figures. As the Weber number decreases, the jet deviates towards a less contracting jet with smaller curvatures at the interface.

For flow with a Weber number of 10, the potential regions of cavitation are shown for Reynolds numbers of 100 and 1000 in figure 13. Comparing these plots with figure 8, reveals a large difference because of surface tension. The pressure on the liquid side of the interface will be smaller owing to the curvature of interface. This causes a larger domain vulnerable to cavitation at lower Weber numbers. Also, since the boundary layer is larger for the lower Reynolds number, the regions of possible cavitation will be larger.

4. Conclusions

The Navier–Stokes equations for the two-dimensional flow of a liquid through an aperture in a flat plate is solved numerically for Reynolds numbers between 1 and 1000. The results are compared to those for viscous potential flow. Funada *et al.*

https://doi.org/10.1017/S0022112008001092 Published online by Cambridge University Press

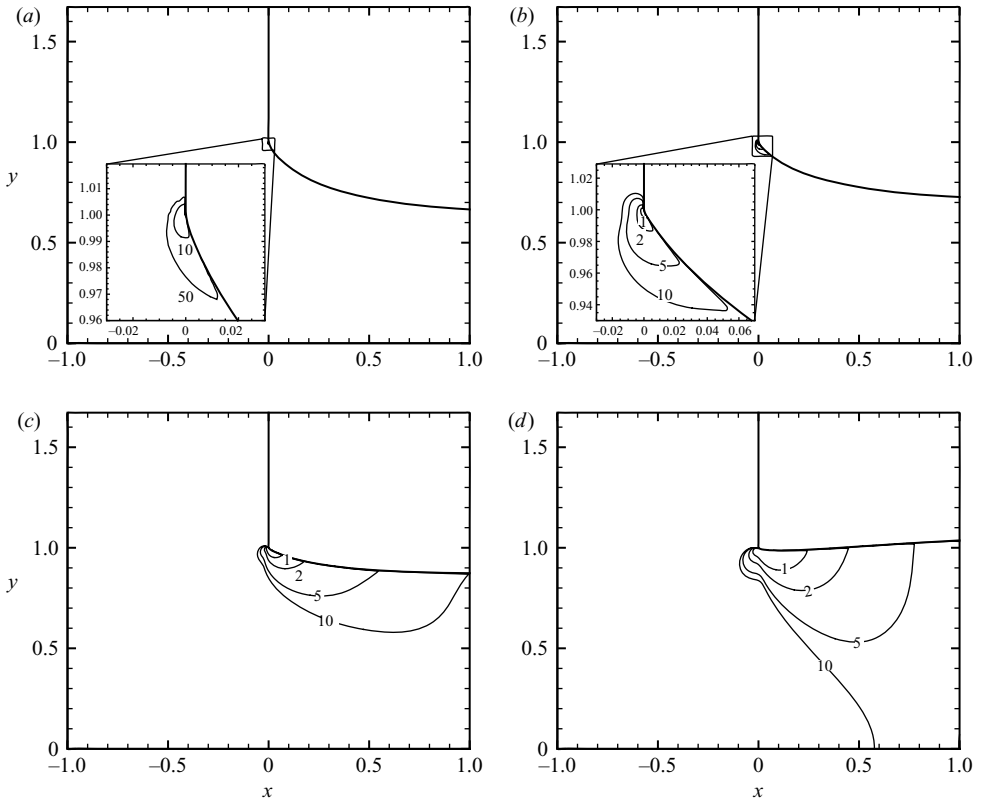


FIGURE 8. Cavitation threshold curves on which $T_{11} + p_c = 0$ in different flows with $K = 1, 2, 5, 10, 50$. ρ-ratio=10^{-4} and μ-ratio $= 10^{-4}$ (*a*) $Re = 1000$, (*b*) 100, (*c*) 10, (*d*) 1.

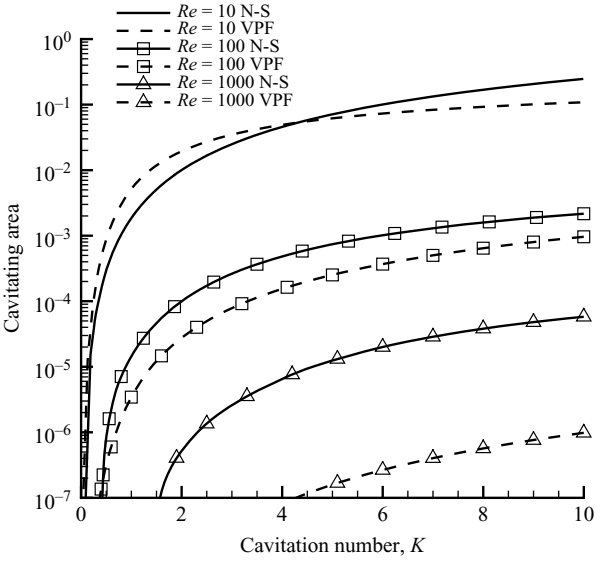


FIGURE 9. Area of cavitating region normalized by L^2: N-S, Navier–stokes; VPF, viscous potential flow.

https://doi.org/10.1017/S0022112008001092 Published online by Cambridge University Press

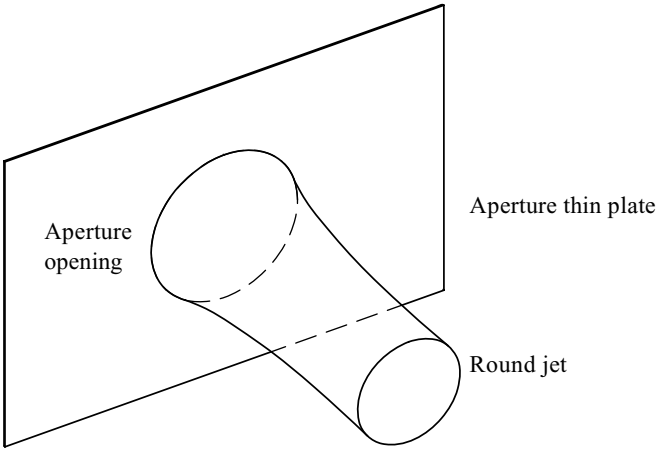


FIGURE 10. Schematic of axisymmetric flow through a round aperture.

(2006) used the free streamline theory of potential flow theory to compute the effects of viscosity in aperture flow. They did not compute the effect of viscous normal stresses on the shape of the streamline. In the Appendix, we show that the classical free streamline theory used by them does not give rise to a normal component of the strain rate; stresses. It follows that this classical free streamline solution cannot give rise to a viscous component of the stress, so that, in fact, there is no change of shape of the free steamline generated by including the effects of viscosity in the potential flow solution. It is still true that free steamline theory neglects the effects of surface tension. At the low Reynolds numbers that have been studied here, the flow is expected to be two-dimensional or axisymmetric. The only cause of three-dimensionality of the flow comes from the inception of cavitation bubbles which breaks the symmetry around the centreline or plane of symmetry. Effects of these disturbances to the flow require further investigations and three-dimensional modelling of the flow.

This research has been supported by the US Army Research Office through grant W911NF-06-1-0225, with Dr Kevin McNesby and Dr Ralph Anthenien having served sequentially as program managers. D. D. J. was also supported by NSF grant CBET-0302837.

Appendix. Boundary condition on normal stress

Here, we shall show that the normal strain rate, the derivative of the normal velocity in the direction normal to the free streamline, vanishes on the free streamline of the potential flow solution used by Funada *et al.* (2006). Therefore, the potential flow with free stream satisfies the boundary condition of the normal stress on the free surface of a viscous flow.

We will take the potential function, ϕ, and streamfunction, ψ, of the potential flow as the orthogonal curvilinear coordinates. The velocity field in this coordinates has a simple form:

$$\left.\begin{array}{ll} x_1 = \phi, & u_1 = q, \\ x_2 = \psi, & u_2 = 0, \end{array}\right\} \tag{A 1}$$

https://doi.org/10.1017/S0022112008001092 Published online by Cambridge University Press

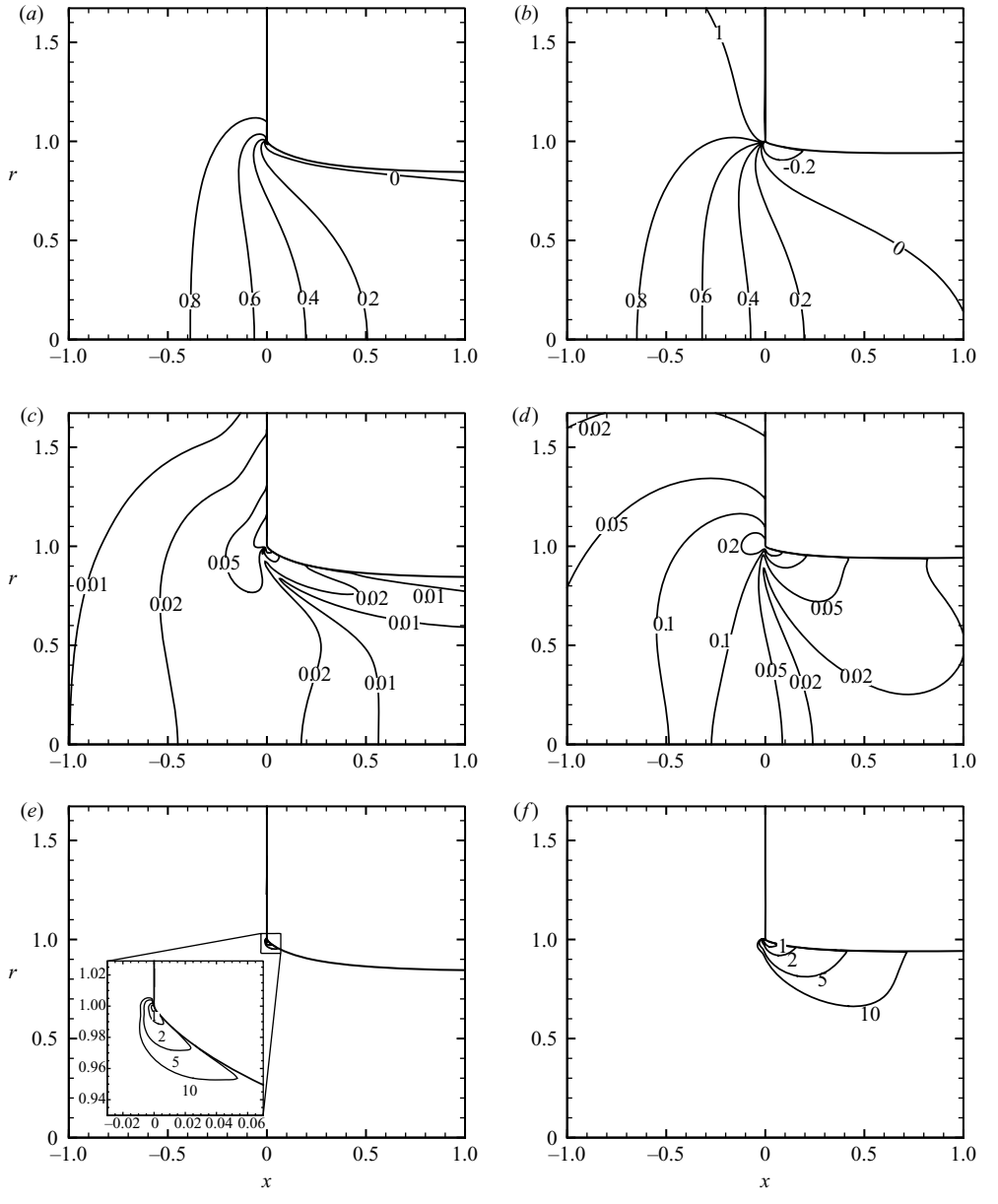


FIGURE 11. Axisymmetric aperture flow; Contours of $(p - p_d)/\frac{1}{2}\rho U^2$ for (*a*) $Re = 100$, (*b*) 10, and maximum principal value of viscous stress for (*c*) $Re = 100$, (*d*) 10, and the cavitation threshold curves on which $T_{11} + p_c = 0$ in different flows with $K = 1, 2, 5, 10$ (*e*) $Re = 100$, (*f*) 10.

where the velocity in the complex domain can be written as:

$$u - \mathrm{i}v = q\mathrm{e}^{-\mathrm{i}\theta}. \tag{A 2}$$

In order to evaluate the stresses, first we define the scale factors:

$$h_1 = h_2 = \frac{1}{\sqrt{u^2 + v^2}} = \frac{1}{q}. \tag{A 3}$$

https://doi.org/10.1017/S0022112008001092 Published online by Cambridge University Press

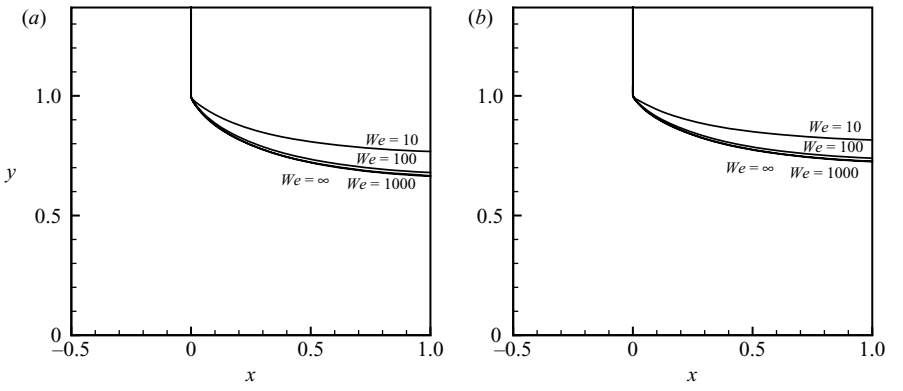


FIGURE 12. Free streamline for planar flows with different Weber numbers, ρ-ratio $= 10^{-4}$ and μ-ratio $= 10^{-4}$ (*a*) $Re = 1000$, (*b*) 100.

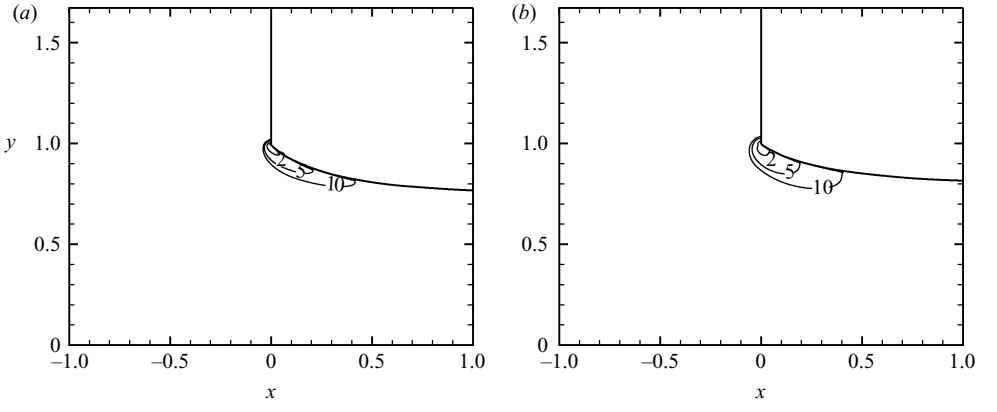


FIGURE 13. Cavitation threshold curves on which $T_{11} + p_c = 0$ in different planar flows with $K = 2, 5, 10$. $We = 10$, ρ-ratio $= 10^{-4}$ and μ-ratio $= 10^{-4}$ (*a*) $Re = 1000$, (*b*) 100.

Calculating the stresses:

$$T_{11} = -p + 2\mu\left[\frac{1}{h_1}\frac{\partial u_1}{\partial x_1} + \frac{u_2}{h_1 h_2}\frac{\partial h_1}{\partial x_2} + \frac{u_3}{h_1 h_3}\frac{\partial h_1}{\partial x_3}\right] = -p + 2\mu q\frac{\partial q}{\partial \phi}, \tag{A 4}$$

$$T_{22} = -p + 2\mu\left[\frac{1}{h_2}\frac{\partial u_2}{\partial x_2} + \frac{u_3}{h_2 h_3}\frac{\partial h_2}{\partial x_3} + \frac{u_1}{h_2 h_1}\frac{\partial h_2}{\partial x_1}\right] = -p - 2\mu q\frac{\partial q}{\partial \phi}, \tag{A 5}$$

$$T_{12} = \mu\left[\frac{h_2}{h_1}\frac{\partial}{\partial x_1}\left(\frac{u_2}{h_2}\right) + \frac{h_1}{h_2}\frac{\partial}{\partial x_2}\left(\frac{u_1}{h_1}\right)\right] = 2\mu q\frac{\partial q}{\partial \psi}. \tag{A 6}$$

Using the Bernoulli equation for viscous potential flow,

$$p_u = p + \frac{1}{2}\rho q^2. \tag{A 7}$$

Now, we can substitute the pressure back in the equations for normal stresses:

$$T_{22} = -p_u + \frac{1}{2}\rho q^2 - 2\mu q\frac{\partial q}{\partial \phi}. \tag{A 8}$$

https://doi.org/10.1017/S0022112008001092 Published online by Cambridge University Press

Along a streamline we have $\mathrm{d}\phi = q\mathrm{d}s$, where $\mathrm{d}s$ is the distance element along the streamline.

$$T_{22} = -p_u + \frac{1}{2}\rho q^2 - 2\mu\frac{\mathrm{d}q}{\mathrm{d}s} \quad \text{along a streamline.} \tag{A 9}$$

Applying the boundary condition:

$$T_{22} = -p_d \quad \Rightarrow \quad \frac{\mathrm{d}q}{\mathrm{d}s} = \frac{1}{2\mu}\rho q^2 - \frac{C}{\mu} \quad \text{along the free streamline,} \tag{A 10}$$

where $C = p_u - p_d$ is the pressure difference between stagnation pressure of the flow and ambient pressure.

Now, we show that for the case of a free jet where s is unbounded, the only possible solution is q = constant. If $\mathrm{d}q/\mathrm{d}s > 0$ initially, then q becomes unbounded, and if $\mathrm{d}q/ds < 0$ initially, then q becomes zero and then negative with increasing s. Both of these situations are non-physical, so the only possible solution happens when $\mathrm{d}q/\mathrm{d}s = 0$ initially, which leads to q = constant. This results in both T_{11} and T_{22} being constant and equal to $-p$ along the free streamline. Therefore, the irrotational flow with constant pressure at the bounding streamline satisfies the viscous boundary condition of normal stress on the free interface. However, it does not satisfy the condition of zero shear stress on the free surface. To develop the shear stress more, we consider the irrotationality condition of the flow in Cartesian coordinates:

$$(\nabla \times \boldsymbol{u})_3 = \frac{\partial v}{\partial x} - \frac{\partial u}{\partial y} \tag{A 11}$$

$$0 = \left(\frac{\partial v}{\partial \psi}\frac{\partial \psi}{\partial x} + \frac{\partial v}{\partial \phi}\frac{\partial \phi}{\partial x}\right) - \left(\frac{\partial u}{\partial \psi}\frac{\partial \psi}{\partial y} + \frac{\partial u}{\partial \phi}\frac{\partial \phi}{\partial y}\right). \tag{A 12}$$

Using the velocity field,

$$u = q\cos\theta, \quad v = q\sin\theta, \tag{A 13}$$

we obtain:

$$(\nabla \times \boldsymbol{u})_3 = -q\frac{\partial q}{\partial \psi} + q^2\frac{\partial \theta}{\partial \phi} = 0, \tag{A 14}$$

which results in:

$$\frac{\partial q}{\partial \psi} = q\frac{\partial \theta}{\partial \phi}. \tag{A 15}$$

Substituting back in (A 6) and using $\mathrm{d}\phi = q\mathrm{d}s$ along a streamline again,

$$T_{12} = 2\mu q\frac{\mathrm{d}\theta}{\mathrm{d}s} = 2\mu q\kappa, \tag{A 16}$$

where κ is the curvature of the streamline. So, in planar irrotational flow, in orthogonal coordinates, one of which is parallel to the streamlines, the shear stress is proportional to the magnitude of velocity multiplied by the curvature of the streamline.

In conclusion, the irrotational flow satisfies the constant normal stress condition on the free surface, but does not satisfy the zero shear stress condition on the free surface and a correction may be necessary.

REFERENCES

Ahn, K., Kim, J. & Yoon, Y. 2006 Effects of orifice internal flow on transverse injection into subsonic crossflows: cavitation and hydraulic flip. *Atomiz. Sprays* **16**, 15–34.

https://doi.org/10.1017/S0022112008001092 Published online by Cambridge University Press

Brown, D. R. 1961 A study of the behaviour of a thin sheet of moving liquid. *J. Fluid Mech.* **10**, 297–305.

Bunnell, R. A. & Heister, S. D. 2000 Three-dimensional unsteady simulation of cavitating flows in injector passages. *Trans. ASME I: J. Fluids I Eng.* **122**, 791–797.

Bunnell, R. A., Heister, S. D., Yen, C. & Collicott, S. H. 1999 Cavitating injector flows: validation of numerical models and simulations of pressure atomizers. *Atomiz. Sprays* **9**, 445–465.

Chen, Y. & Heister, S. D. 1996 Modeling cavitating flows in diesel injectors. *Atomiz. Sprays* **6**, 709–726.

Currie, I. G. 1974 *Fundamental Mechanics of Fluids*. McGraw-Hill.

Dabiri, S., Sirignano, W. A. & Joseph, D. D. 2007 Cavitation in an orifice flow. *Phys. Fluids* **19** (7), 072112.

Funada, T., Wang, J. & Joseph, D. D. 2006 Viscous potential flow analysis of stress induced cavitation in an aperture flow. *Atomiz. Sprays* **16**, 763–776.

Ganippa, L. C., Bark, G., Andersson, H. I. & Chomiak, J. 2004 Cavitation: a contributory factor in the transition from symmetric to asymmetric jets in cross-flow nozzles. *Exp. Fluids* **36**, 627–634.

Hayase, T., Humphrey, J. A. C. & Greif, R. 1992 A consistently formulated quick scheme for fast and stable convergence using finite-volume iterative calculation procedure. *J. Comput. Phys.* **98**, 108–118.

He, L. & Ruiz, F. 1995 Effect of cavitation on flow and turbulence in plain orifices for high-speed atomization. *Atomiz. Sprays* **5**, 569–584.

Hiroyasu, H. 2000 Spray breakup mechanism from the hole-type nozzle and its applications. *Atomiz. Sprays* **10**, 511–527.

Hirt, C. W. & Nichols, B. D. 1981 Volume of fluid (VOF) method for the dynamics of free boundaries. *J. Comput. Phys.* **39**, 201–225.

Joseph, D. D. 1998 Cavitation and the state of stress in a flowing liquid. *J. Fluid Mech.* **366**, 367–376.

Joseph, D. D. & Wang, J. 2004 The dissipation approximation and viscous potential flow. *J. Fluid Mech.* **504**, 365–377.

Jung, K., Khil, T. & Yoon, Y. 2006 Effects of orifice internal flow on breakup characteristic of like-doublet injectors. *J. Propul. Power* **22**, 653–660.

Kubota, A., Kato, H. & Yamaguchi, H. 1992 A new modeling of cavitating flows a numerical study of unsteady cavitation on a hydrofoil. *J. Fluid Mech.* **240**, 59–96.

Lefebvre, A. H. 1989 *Atomization and Sprays*. Hemisphere.

Middleman, S. & Gavis, J. 1961 Expansion and contraction of capillary jets of Newtonian liquids. *Phys. Fluids* **4** (3), 355–359.

Mishra, C. & Peles, Y. 2005*a* Cavitation in flow through a micro-orifice inside a silicon microchannel. *Phys. Fluids* 013601.

Mishra, C. & Peles, Y. 2005*b* Flow visualization of cavitating flows through a rectangular slot micro-orifice ingrained in a microchannel. *Phys. Fluids* **17** (11), 113602.

Moore, D. W. 1965 The velocity of rise of distorted gas bubbles in a liquid of small viscosity. *J. Fluid Mech.* **23**, 749–766.

Nurick, W. H. 1976 Orifice cavitation and its effect on spray mixing. *Trans. ASME I: J. Fluids Eng.* **98**, 681–687.

Osher, S. & Fedkiw, R. P. 2001 Level set methods: an overview and some recent results. *J. Comput. Phys.* **169**, 436.

Padrino, J. C., Joseph, D. D., Funada, T., Wang, J. & Sirignano, W. A. 2007 Stress-induced cavitation for the streaming motion of a viscous liquid past a sphere. *J. Fluid Mech.* **578**, 381–411.

Patankar, S. V. 1980 *Numerical Heat Transfer and Fluid Flow*. Hemisphere.

Payri, F., Bermudez, V., Payri, R. & Salvador, F. J. 2004 The influence of cavitation on the internal flow and the spray characteristics in diesel injection nozzles. *Fuel* **83**, 419–431.

Popinet, S. & Zaleski, S 1999 A front-tracking algorithm for accurate presentation of surface tension. *Intl J. Numer. Meth. Fluids* **30**, 775–793.

Scardovelli, R. & Zaleski, S. 1999 Direct numerical simulation of free-surface and interfacial flow. *Annu. Rev. Fluid Mech.* **31**, 567–603.

https://doi.org/10.1017/S0022112008001092 Published online by Cambridge University Press

Sussman, M., Fatemi, E., Smereka, P. & Osher, S. 1998 An improved level set method for incompressible two-phase flows. *Comput. Fluids* **27**, 663–680.

Tamaki, N., Shimizu, M., Nishida, K. & Hiroyasu, H. 1998 Effects of cavitation and internal flow on atomization of a liquid jet. *Atomiz. Sprays* **8**, 179–197.

Tamaki, N., Shimizu, M. & Hiroyasu, H. 2001 Enhancement of the atomization of a liquid jet by cavitation in a nozzle hole. *Atomiz. Sprays* **11**, 125.

Tryggvason, G., Bunner, B., Esmaeeli, A., Juric, D., Al-Rawahi, N., Tauber, W., Han, J., Nas, S. & Jan, Y. J. 2001 A front-tracking method for the computations of multiphase flow. *J. Comput. Phys.* **169**, 708–759.

Xu, C., Heister, S. D. & Blaisdell, G. A. 2004 Simulation of cavitated flow in orifices fed by a manifold. *Atomiz. Sprays* **14**, 37–52.

https://doi.org/10.1017/S0022112008001092 Published online by Cambridge University Press